J. Fluid Mech. (2005), *vol.* 532, *pp.* 217–242.
doi:10.1017/S0022112005004027 Printed in the United Kingdom

On undercompressive shocks and flooding in countercurrent two-layer flows

By T. M. SEGIN[1]†, B. S. TILLEY[2] AND L. KONDIC[1]

[1]Department of Mathematical Sciences and Center for Applied Mathematics and Statistics, New Jersey Institute of Technology, Newark, NJ 07102, USA

[2]Franklin W. Olin College of Engineering, Olin Way, Needham, MA 02492, USA

(Received 6 December 2003 and in revised form 4 January 2005)

We consider the countercurrent flow of two incompressible immiscible viscous fluids in an inclined channel. This configuration may lead to the phenomena of 'flooding', i.e. the transition from a countercurrent regime to a cocurrent regime. This transition is marked by a variety of transient behaviour, such as the development of large-amplitude waves that impede the flow of one of the fluids to the reversal of the flow of the denser fluid. From a lubrication approximation based on the ratio of the channel height to the downstream disturbance wavelength, we derive a nonlinear system of evolution equations that govern the interfacial shape separating the two fluids and the leading-order pressure. This system, which assumes fluids with disparate density and dynamic viscosity ratios, includes the effects of viscosity stratification, inertia, shear and capillarity. Since the experimental constraints for this effective system are unclear, we consider two ways to drive the flow: either by fixing the volumetric flow rate of the gas phase or by fixing the total pressure drop over a downstream length of the channel. The latter forcing results in a single evolution equation whose dynamics depends non-locally on the interfacial shape. From both of these driven systems, admissible criteria for Lax shocks, undercompressive shocks and rarefaction waves are investigated. These criteria, through a numerical verification, do not depend significantly on the inertial effects within the more dense layer. The choice of the local/non-local constraints appears to play a role in the transient growth of undercompressive shocks, and may relate to the phenomena observed near the onset of flooding.

1. Introduction

Liquid films are encountered in many physical situations. Examples of their practical application include condensate flow in gas wells (Duenckel 2002), oil and gas flow through sub-sea tiebacks (Moritis 2001), or in the on-chip cooling of micro-electromechanical (MEMS) devices (Pettigrew *et al.* 2001). Two-phase gas–liquid flows are also important in a number of space operations including the design and operation of spacecraft environmental systems, storage and transfer of cryogenic fluids and safety and performance issues related to space nuclear power systems (Dukler *et al.* 1988; Bousman, McQuillen & Witte 1996). In this work, we consider the separated two-phase gas–liquid scenario shown in figure 1. A liquid layer is driven down along the left-hand wall by gravity, while an adverse pressure gradient moves the gas in

† Present address: Department of Chemical and Materials Engineering, University of Alberta, Edmonton, Alberta, Canada T6G 2G6.

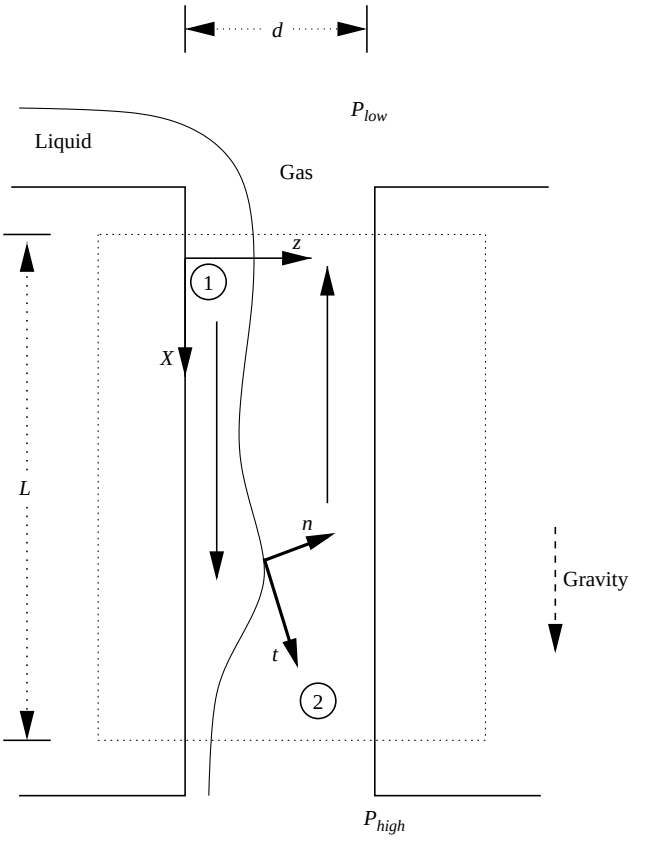

FIGURE 1. Outline of the problem of interest. The plate on the left-hand side is coated by a liquid driven by gravity (pointing down), while the gas is driven by an adverse pressure drop (higher pressure at the liquid exit). This system, even in isothermal conditions, can undergo hydrodynamic instabilities for sufficiently large adverse pressure drops. In this work, we consider only the domain in the dashed box, and we do not consider the entrance or exit effects in the liquid or the gas. The local coordinate frame, based on the channel, is also shown.

the opposite direction. In applications, the transfer of heat is from the liquid-coated surface into the liquid. The heat is then carried by the liquid down the plate, and is conducted through the liquid into the gas. The gas then carries the heat away through advection from the application to the environment. Hence, heat-transfer rates are improved as the gas flow rate increases.

Even in isothermal situations, the increase of the adverse pressure drop results in hydrodynamic instabilities. The two fluids can flow either cocurrently (both fluids flow in the same direction) or countercurrently (fluids flow in opposite directions). The transition from the countercurrent flow shown in figure 1 to a cocurrent flow adverse to gravity as the adverse pressure drop is increased is called *flooding*. Two examples of phenomena which are considered as flooding are: (i) large interfacial deformations of the liquid that prevents the flow of gas, and (ii) transition during which the liquid flow rate is reduced or inverted. Flooding has been investigated extensively both phenomenologically (Chang 1986; Fowler & Lisseter 1992) and experimentally (see Bankoff & Lee (1986) and the references therein), but the criteria for onset of flooding are still an open question. It is known, however, that during the transition

from countercurrent to cocurrent upstream flow, a whole range of waves is observed, from possibly chaotic small-amplitude ones to large-amplitude waves that impede the flow of the gas. Countercurrent flow returns only after the pressure gradient is decreased below the flooding point. One of our goals in this paper is to discuss possible connections between the complicated interfacial dynamics and the onset of flooding. There are several physical mechanisms that play a role in this description, and a brief outline of these mechanisms follows.

If the gas layer is considered passive, then the dynamics of the interface is driven purely by gravitational, inertial and capillary forces. The long-wave linear stability theory for single thin liquid films was developed by Benjamin (1957). At small angles of inclination, Floryan, Davis & Kelly (1987) studied a falling single-phase film and found that the growth rates of a disturbance could be reduced by increasing the surface tension or decreasing the angle of inclination. They also reported that the critical Reynolds number (Re) of the shear mode varied non-monotonically with either the inclined angle or surface tension parameter. Smith (1990) used the model of a thin liquid film with deformable top (right-hand wall in figure 1) surface flowing down a rigid inclined plane to discuss the mechanisms for instability: initiating mechanism (shear and/or velocity induced) that drives the dominant motion in a perturbed film, and growth mechanism (due to inertial stress) that produces the unstable motion of the interface. Joo, Davis & Bankoff (1991) found that waves can steepen and increase in height to a range where the long-wave assumptions cease to be valid. When the disturbance wavenumber is sufficiently small, a numerical solution of the evolution equation shows that the wave grows initially at the exponential rate of linear theory, but later grows super-exponentially. Peaks grow much faster than troughs deepen, and the front of the peak steepens toward the vertical, showing the incipient breaking, and the second trough grows behind the peak. Chang (1986) used a phenomenological model to investigate the interfacial behaviour of two-phase flow under the assumption of a passive upper phase and allowed turbulent shear stress on the interface.

For the case of two-layer flow, the initiating mechanism for the long-wave instability is richer than that for the single layer (due to viscosity and/or density stratification). Linear stability of two superposed layers of fluids was first studied by Yih (1967) for the plane Couette–Poiseuille flow in a horizontal channel. Using a long-wave assumption, he showed that the interface was susceptible to instability owing to the viscosity stratification. A summary of the mathematical theory for two-layer flows and core–annular flows can be found in Joseph & Renardy (1992). Core–annular flows are found in vertical tubes in which one fluid forms the 'core', centred on the tube axis, while the other fluid form an annulus between the core and the tube wall. Two-phase cocurrent (both phases flow in the same direction) core–annular flow of air and water was extensively studied by Kouris & Tsamopoulos (2002) in a host of geometries ranging from model arrangements to single vertical constricted tubes. The ratio of viscosity of the fluid in the annulus to that in the core of the tube, μ, is greater than or equal to one. They found that the difference in viscosity of the two fluids induces an interfacial velocity, which is directly responsible for the transition from chaotic interactions obtained for viscosity ratio close to one, to well-organized wavetrains obtained for large values of μ. The viscosity ratio does not, however, affect the long-time behaviour of the wave shape and wave amplitude. The increase in the effect of surface tension causes a proportional increase in the amplitude of the resulting wave in addition to the fact that it reduces the wave speed drastically. For larger values of μ, the initial condition does not determine whether the interfacial shapes are chaotic or organized in space and time.

Tilley, Davis & Bankoff (1994*a*) investigated the influence of the channel thickness and the mean interfacial height on the stability of two-layer superposed fluid flow, and identified the mechanisms for linear stability in the long-wave limit where the flow rate of each layer is prescribed. Gravity-driven flow of two incompressible immiscible viscous fluids on a periodic spatial domain was studied numerically as a fully nonlinear free-boundary problem by Zhang *et al.* (2002). It was found that wave crests were formed as unstable waves flowing downstream. It was observed that increasing the viscosity of the upper fluid, and decreasing the angle of inclination made the flow more stable. Their conclusion is similar to the results in Floryan *et al.* (1987). The attempt to classify the instabilities in parallel two-phase flow is made in Boomkamp & Miesen (1996). The criteria for dividing the mechanisms of instabilities into classes is based on how the energy is being transferred from the primary to the disturbed flow. These mechanisms find their origin in one of the following properties of the flow system: density stratification and orientation (Rayleigh–Taylor and instability induced by tangential disturbances, i.e. viscosity and/or gravity instabilities), velocity profile curvature (Miles instability), viscosity stratification, shear effects or a combination of the last two effects.

All models discussed above were investigated under the assumption of constant flow-rate constraints. An alternative constraint is to fix the pressure drop over the length of the channel. An additional motivation for considering this constraint is that in experiments and applications it is very difficult to maintain a constant flow rate, especially when the upper fluid is a gas. Thus, in this paper we consider two-fluid systems in both regimes and discuss the differences.

Finally, we consider a system in which an interfacial shear stress acts in the direction opposite to gravity. A single-phase falling liquid film on an inclined substrate can be driven up the plate by, for example, Marangoni-induced shear stresses induced by an appropriate temperature gradient. These films are considered for applications involving selective wetting in a lab-on-a-chip set-up (see Kataoka & Troian 1999; Stone, Stroock & Ajdari 2004). Until recently, it was believed that for such systems only compressive shocks (in which characteristics enter the shock from each side) occur. However, recently, it has been discovered that the interfacial dynamics of these films includes the development of undercompressive shocks. There is also a growing amount of theoretical work indicating that undercompressive shocks are observed in other physical systems. Kluwick, Cox & Scheichl (2000) find these waves in a modified Korteweg–de Vries–Burgers equation which describes the evolution of weakly nonlinear concentration waves in suspensions of particles in fluids. Mathematically, the advancing front of a driven film is an important example of shock formation in a system described by a scalar conservation law.

The first indication of this more complicated interfacial dynamics comes from the comparison of two series of experiments. The first experimental investigation of this particular thin-film behaviour was done by Ludviksson & Lightfoot (1971). Using squalane oil spreading on a silver substrate, with surface stresses of the order of $0.2\,\mathrm{dyn\,cm^{-2}}$ or less, produces stable spreading films with a straight-edged moving front. Using interferometry, they reconstruct the film thickness profiles and show that the film shape decreases monotonically toward the substrate with no evidence of a capillary rim at the advancing front. In contrast, Carles & Cazabat (1993) report a well-formed fingering instability at the leading edge of a climbing film which develops within minutes of applying a vertical temperature gradient. In these experiments, a silicone oil film, subject to stresses of approximately $0.5\,\mathrm{dyn\,cm^{-2}}$ and higher, is made to coat a silicon wafer. This 'contradiction' between the results of Ludviksson &

Lightfoot (1971) and Carles & Cazabat (1993) inspired a number of new analytical and experimental studies (Bertozzi *et al.* 1998; Bertozzi, Münch & Shearer 1999). Bertozzi *et al.* (1998) observe experimentally the formation of a very large capillary ridge. The ridge continues to broaden as it advances up the plate. Despite the large capillary ridge, the contact line remains stable. Bertozzi *et al.* (1998) emphasize that undercompressive shock plays a key role in preventing the contact line from fingering (i.e. breaking up into rivulets). Schneemilch & Cazabat (2000*a*) show experimentally that this undercompressive shock (for which characteristics enter the shock on one side and leave on the other) for infinite films and substrates can be applied to real systems of finite dimensions. These experiments stimulate new theory for these problems resulting in discovery of reverse undercompressive shock (Münch 2003; Sur, Bertozzi & Behringer 2003). The reverse undercompressive shock forms the trailing edge of a double shock wave in a thin liquid film that moves up the wafer. The velocity of the wave and the thickness of the enclosed film can be varied by changing the temperature gradient or the inclination angle, and the total amount of fluid can be changed by modifying the initial conditions. This shock is reversed because it involves a thicker film advancing upward from a thinner film, which is the reverse of the type found by Schneemilch & Cazabat (2000*b*).

In this paper, we discuss analytically and numerically the dynamics of the interface in a two-fluid system, and find the formation of the waves that, for the constant gas flow-rate case, are similar to those found in the one-fluid flow discussed above. This similarity is used to classify the dynamics found in the constant pressure-drop case, where travelling-wave solutions are typically not found.

The structure of this paper is as follows. In § 2, we formulate the problem, discuss the assumptions that we use, and derive the highly nonlinear evolution equation. Section 3 describes the numerical method. In § 4, necessary, but not sufficient conditions for the existence of weak travelling-wave solutions are investigated. We find the regions of their existence for constant gas volumetric flow rate, and the four cases of solutions found in Bertozzi *et al.* (1999) are present in our problem as well. In § 5, we verify numerically our analytical results and find that the structure of the interfacial profile for given system parameters (ratio of densities, dynamical viscosities, etc.) for the constant gas volumetric flow-rate case, involves the Lax (classical) shock, double shock (Lax and undercompressive) and combination of rarefaction wave with undercompressive shock. For an applied fixed pressure drop across the channel, we find that the maximum height of these dynamics grow in time. Inertial effects are also discussed. We draw conclusions in § 6.

2. Formulation and governing equations

Consider the flow of two viscous incompressible fluids in a channel of height d and length L (figure 1), where $\boldsymbol{n}$ is the unit normal pointing from phase 1 into phase 2, and $\boldsymbol{t}$ is the unit tangent vector at the interface. The equations that govern this system are continuity and Navier–Stokes (asterisks denote dimensional variables):

$$\bar{\nabla}\cdot\boldsymbol{u}^{*(i)} = 0,$$

$$\rho_i^*\left(\frac{\partial \boldsymbol{u}^{*(i)}}{\partial t^*} + \boldsymbol{u}^{*(i)}\cdot\bar{\nabla}\boldsymbol{u}^{*(i)}\right) = -\bar{\nabla}p^{*(i)} + \rho_i^*\boldsymbol{g} + \mu_i^*\bar{\nabla}^2\boldsymbol{u}^{*(i)}.$$

The superscript (i) on the dependent variables correspond to $i=2$ – upper fluid and $i=1$ – lower fluid, respectively, with corresponding densities ρ_i^*, dynamic viscosities μ_i^*

and pressures $p^{*(i)}$. The velocities $\boldsymbol{u}^{*(i)} = (u^{*(i)}, w^{*(i)})$ satisfy these boundary conditions on the channel walls: $\boldsymbol{u}^{*(1)} = 0$ at $z^* = 0$ and $\boldsymbol{u}^{*(2)} = 0$ at $z^* = d$, as well as the balance of normal stress, balance of tangential stress, continuity of normal and tangential components of velocity and kinematic condition at $z^* = h^*(x^*, t^*)$:

$$[\boldsymbol{n} \cdot \boldsymbol{T}^* \cdot \boldsymbol{n}] = \sigma^* \kappa^*, \tag{2.1}$$

$$[\boldsymbol{t} \cdot \boldsymbol{T}^* \cdot \boldsymbol{n}] = 0, \tag{2.2}$$

$$[\boldsymbol{u}^* \cdot \boldsymbol{n}] = 0, \tag{2.3}$$

$$[\boldsymbol{u}^* \cdot \boldsymbol{t}] = 0, \tag{2.4}$$

$$h^*_{t^*} + u^* h^*_{x^*} - w^* = 0, \tag{2.5}$$

where the jump $[f]$ of the quantity f across the interface is denoted by $[f] = f^{(2)} - f^{(1)}$. $\boldsymbol{T}^*$ denotes the stress tensor, σ^* is the surface tension between the two fluids, and κ^* is twice the mean curvature of the interface, given by

$$\kappa^* = -h^*_{x^* x^*} \left(1 + h^{*2}_{x^*}\right)^{-3/2}.$$

We scale lengths by d, time by ν_1^*/dg, densities by ρ_1^* and velocities by $d^2 g/\nu_1^*$, where ν_1^* is the kinematic viscosity of the lower fluid. That determines the pressure scale as $\rho_1^* dg$. Thus, we obtain

$$\nabla \cdot \boldsymbol{u}^{(i)} = 0, \tag{2.6}$$

$$Re_l \frac{\rho_i^*}{\rho_1^*} \left[\frac{\partial \boldsymbol{u}^{(i)}}{\partial t} + \boldsymbol{u}^{(i)} \cdot \nabla \boldsymbol{u}^{(i)} \right] = -\nabla p^{(i)} + \frac{\rho_i^*}{\rho_1^*} \hat{\boldsymbol{g}} + \frac{\mu_i^*}{\mu_1^*} \nabla^2 \boldsymbol{u}^{(i)}, \tag{2.7}$$

where $Re_l = gd^3/\nu_1^{*2}$ is the Reynolds number of the lower fluid, $\hat{\boldsymbol{g}}$ is the unit vector in the direction of gravity and velocities are $\boldsymbol{u}^{(i)} = (u^{(i)}, w^{(i)})$.

The boundary conditions on the channel walls become: $\boldsymbol{u}^{(1)} = 0$ on $z = 0$ and $\boldsymbol{u}^{(2)} = 0$ on $z = 1$. The conditions (2.1)–(2.5) at $z = h(x, t)$ become

$$[\boldsymbol{n} \cdot \boldsymbol{T} \cdot \boldsymbol{n}] = \sigma \kappa, \tag{2.8}$$

$$[\boldsymbol{t} \cdot \boldsymbol{T} \cdot \boldsymbol{n}] = 0, \tag{2.9}$$

$$[\boldsymbol{u} \cdot \boldsymbol{n}] = 0, \tag{2.10}$$

$$[\boldsymbol{u} \cdot \boldsymbol{t}] = 0, \tag{2.11}$$

$$h_t + u h_x - w = 0. \tag{2.12}$$

where

$$\sigma = \frac{\sigma^*}{\rho_1 d^2 g}.$$

We are interested in gas–liquid systems where the density and dynamic viscosity ratios are small. Following the case of air–water (under standard conditions: $\rho_2^*/\rho_1^* = 8 \times 10^{-4}$, $\mu_2^*/\mu_1^* = 2 \times 10^{-2}$), we assume that $\bar{\rho} = \rho_2^*/\rho_1^*$ is of order ϵ^2 and $\bar{\mu} = \mu_2^*/\mu_1^*$ is of order ϵ, where ϵ is an aspect ratio of channel thickness to a characteristic channel length, i.e. $\bar{\rho} = \epsilon^2 \rho$, $\bar{\mu} = \epsilon \mu$, and ρ, μ are $O(1)$. This distinguished limit allows us to capture the dominant physical effects in this system, while simplifying the analysis considerably, as we will see below. For an air–water system, this scaling is consistent with experiments performed in the channels several hundred microns wide (see, e.g. Pettigrew *et al.* 2001).

In terms of the Reynolds numbers for the liquid and the gas, if U_l is the characteristic velocity of the liquid, and U_g is the characteristic velocity of the gas, then the ratio

of the liquid Reynolds number to the gas Reynolds number is given by

$$\frac{Re_l}{Re_g} = \frac{dU_l/\nu_1^*}{dU_g/\nu_2^*} = \frac{\nu_2^*}{\nu_1^*}\frac{U_l}{U_g} = \frac{1}{\epsilon}\frac{U_l}{U_g}.$$

Therefore, the characteristic gas velocity scale is $O(U_l/\epsilon)$ since we consider that $Re_g = Re_l = O(1)$.

Next, we assume that changes of the flow occur on a spatial scale that is much longer than the channel thickness. Therefore, we use scaled variables $\xi = \epsilon x$ and $\zeta = z$. The kinematic boundary condition (2.12) then requires rescaling of time as $\tau = \epsilon t$.

Assume a regular perturbation expansion for u in ϵ:

$$u^{(1)}(\xi, \zeta, \tau) = u_0^{(1)}(\xi, \zeta, \tau) + \epsilon u_1^{(1)}(\xi, \zeta, \tau) + \cdots.$$

and then from the continuity equation (2.6), it follows that

$$w^{(1)}(\xi, \zeta, \tau) = \epsilon\{w_0^{(1)}(\xi, \zeta, \tau) + \epsilon w_1^{(1)}(\xi, \zeta, \tau) + \cdots\}.$$

For the gas, the asymptotic expansion for the tangential velocity is

$$u^{(2)}(\xi, \zeta, \tau) = \frac{1}{\epsilon}\{u_0^{(2)}(\xi, \zeta, \tau) + \epsilon u_1^{(2)}(\xi, \zeta, \tau) + \cdots\}.$$

From the continuity equation (2.6):

$$w^{(2)}(\xi, \zeta, \tau) = w_0^{(2)}(\xi, \zeta, \tau) + \epsilon w_1^{(2)}(\xi, \zeta, \tau) + \cdots.$$

Since the system is driven by a pressure gradient and possibly gravity, we expect from balancing terms in (2.7) that the downstream pressure gradients will be of unit order:

$$p^{(i)}(\xi, \zeta, \tau) = \frac{1}{\epsilon}\{p_0^{(i)}(\xi, \zeta, \tau) + \epsilon p_1^{(i)}(\xi, \zeta, \tau) + \cdots\} \qquad (i = 1, 2). \tag{2.13}$$

Based on the experimental configurations involving micrometric channels, (see, e.g. Pettigrew *et al.* 2001), we let the capillary forces be large compared to hydrostatic forces; therefore, we define the unit-order parameter $S = \epsilon^2\sigma$.

Next, we proceed to asymptotically expand the governing equations in orders of ϵ. Note that a similar expansion was performed by Tilley, Davis & Bankoff (1994*b*) without our particular scaling of viscosities and densities. Therefore, their formulation is applicable to a wider range of fluid combinations than that derived here, but also significantly more involved algebraically.

We obtain from (2.6)–(2.12) a sequence of linear problems:

$O(\epsilon^{-1})$:
$$p_{0\zeta}^{(i)} = 0, \tag{2.14}$$
$$p_0^{(1)} = p_0^{(2)} \qquad (\zeta = h(\xi, \tau)), \tag{2.15}$$
$$u_0^{(2)} = 0 \qquad (\zeta = h(\xi, \tau)), \tag{2.16}$$

$O(1)$:
$$-p_{0\xi}^{(2)} + \mu u_{0\zeta\zeta}^{(2)} = 0, \tag{2.17}$$
$$-p_{0\xi}^{(1)} + \sin\beta + u_{0\zeta\zeta}^{(1)} = 0, \tag{2.18}$$
$$p_{1\zeta}^{(1)} + \cos\beta = 0, \tag{2.19}$$
$$p_{1\zeta}^{(2)} = 0, \tag{2.20}$$
$$u_{0\xi}^{(1)} + w_{0\zeta}^{(1)} = 0, \tag{2.21}$$

$$O(1): \qquad u_{0\xi}^{(2)} + w_{0\zeta}^{(2)} = 0, \tag{2.22}$$

$$u_1^{(2)} - u_0^{(1)} = 0 \qquad (\zeta = h(\xi, \tau)), \tag{2.23}$$

$$\mu u_{0\zeta}^{(2)} - u_{0\zeta}^{(1)} = 0 \qquad (\zeta = h(\xi, \tau)), \tag{2.24}$$

$$p_1^{(1)} - p_1^{(2)} = -Sh_{\xi\xi} \quad (\zeta = h(\xi, \tau)), \tag{2.25}$$

$$w_0^{(2)} - h_\xi u_0^{(2)} = 0 \qquad (\zeta = h(\xi, \tau)), \tag{2.26}$$

$$u_0^{(1)} = 0 \qquad (\zeta = 0), \tag{2.27}$$

$$u_0^{(2)} = 0 \qquad (\zeta = 1), \tag{2.28}$$

$$w_0^{(1)} = 0 \qquad (\zeta = 0), \tag{2.29}$$

$$w_0^{(2)} = 0 \qquad (\zeta = 1). \tag{2.30}$$

From equations $O(\epsilon^{-1})$ we find that

$$p_0^{(1)}(\xi, \tau) = p_0^{(2)}(\xi, \tau) = p_0(\xi, \tau).$$

The $O(1)$ z-momentum equations (2.19) and (2.20) with condition (2.25) on the interface yield

$$p_1^{(1)}(\xi, \zeta, \tau) = -\cos\beta\zeta + P_1(\xi, \tau),$$

and

$$p_1^{(2)}(\xi, \tau) = -h(\xi, \tau)\cos\beta + P_1(\xi, \tau) + Sh_{\xi\xi}. \tag{2.31}$$

We refer to $P_1(\xi, \tau)$ as the pressure correction in what follows.

The $O(1)$ x-momentum equations (2.17), (2.18), the continuity equations (2.21), (2.22) with boundary conditions (2.27)–(2.30), and continuity of tangential component of the velocity and shear stress at interface (2.16), (2.24) yield

$$u_0^{(1)} = \frac{p_{0\xi} - \sin\beta}{2}\zeta^2 + \frac{2h\sin\beta - (h+1)p_{0\xi}}{2}\zeta, \tag{2.32}$$

$$w_0^{(1)} = -\frac{p_{0\xi\xi}}{6}\zeta^3 + \left\{-h_\xi \sin\beta + \frac{p_{0\xi\xi}}{2}(h+1) + p_{0\xi}\frac{h_\xi}{2}\right\}\frac{\zeta^2}{2}, \tag{2.33}$$

$$u_0^{(2)} = \frac{p_{0\xi}}{2\mu}(\zeta - 1)^2 + \frac{p_{0\xi}(1-h)}{2\mu}(\zeta - 1), \tag{2.34}$$

$$w_0^{(2)} = -\frac{p_{0\xi\xi}}{6\mu}(\zeta - 1)^3 + \frac{(p_{0\xi}\,[h-1])_\xi}{4\mu}(\zeta - 1)^2. \tag{2.35}$$

The details of this procedure at $O(\epsilon)$ are given in Appendices A and B. From this analysis, we obtain a coupled nonlinear system of equations describing the evolution of the interface and the pressure gradient

$$h_\tau + A_1(h, p_{0\xi})h_\xi + \epsilon[SC(h)h_{\xi\xi\xi} + A_2(h, p_{0\xi}) + Re_l I(h, p_{0\xi}) + P(h)h_\xi]_\xi = 0, \tag{2.36}$$

$$[p_{0\xi}(1-h)^3]_\xi = 0, \tag{2.37}$$

where

$$A_1(h, p_{0\xi}) = h^2\sin\beta - \frac{h(h+1)}{2(1-h)}p_{0\xi}, \tag{2.38}$$

$$C(h) = \tfrac{1}{3}h^3, \quad P(h) = -\tfrac{1}{3}h^3\cos\beta,$$

$$A_2(h, p_{0\xi}) = \frac{\mu h^3 p_{0\xi}}{4(1-h)} + \frac{\mu h^4}{4(h-1)} \sin\beta + \frac{\mu h^2(h+3)}{(1-h)^3}\left[\gamma - \frac{h^2(h+3)}{12}\sin\beta - \frac{h(h-1)}{4}p_{0\xi}\right],$$

$$I(h, p_{0\xi}) = I_l + I_g,$$

with

$$I_l = \frac{h^4(7h+25)}{240} p_{0\xi\tau} + \frac{h^5 h_\xi}{15}\left\{2h\sin^2\beta + \frac{56+49h-41h^2}{56(h-1)}p_{0\xi}\sin\beta + \frac{(10h^2+7h+77)}{224(h-1)}p_{0\xi}^2\right\}, \quad (2.39)$$

$$I_g = \frac{\rho h^2(1-h)^3 h_\xi p_{0\xi}^2}{480\mu^2}\left\{\frac{17(h+3)}{7} + 13(1-h)\right\}, \quad (2.40)$$

and

$$\gamma = \int_0^\xi \frac{h(h+1)h_{\hat\xi} p_{0\hat\xi}}{2(1-h)}\,\mathrm{d}\hat\xi + C_1. \quad (2.41)$$

The expression for γ (including C_1) is discussed in §4. The second term in the evolution equation corresponds to advection effects and consists of two sub-terms: the first one describes wave propagation and steepening and the second describes the influence of pressure gradient. The third, fourth and fifth terms in the evolution equation describe capillary, inertia and hydrostatic effects. In the inertial term, I_l corresponds to the inertial effects within the liquid, while I_g corresponds to inertial effects of the gas. In this work, the dynamics of interest corresponds to a weak adverse pressure drop (I_g small).

Integrating (2.37) with respect to ξ gives

$$p_{0\xi} = \frac{\Phi(\tau)}{(1-h)^3}.$$

In order to find $\Phi(\tau)$, let us introduce the gas volumetric flow rate $q(\tau)$:

$$q(\tau) = \int_h^1 u^{(2)}\,\mathrm{d}\zeta.$$

Then after substituting (2.34), we obtain

$$q(\tau) = -\frac{(1-h)^3}{12\mu}p_{0\xi}, \qquad \Phi(\tau) = -12\mu q(\tau). \quad (2.42)$$

At this stage, we can either require that $q(\tau)$ is fixed, and $p_{0\xi}$ is found explicitly in terms of the interfacial shape, or that the pressure drop $\Delta P = p_0(0) - p_0(1)$ is fixed. In the latter case, after integrating (2.37) we obtain

$$\Delta P = 12\mu q(\tau)\int_0^L \frac{\mathrm{d}\xi}{(1-h)^3}.$$

Then in terms of an imposed pressure drop, ΔP, the equation for the pressure gradient becomes

$$p_{0\xi} = -\frac{\Delta P}{(1-h)^3\displaystyle\int_0^L (\mathrm{d}\xi/(1-h)^3)}. \quad (2.43)$$

Theoretical works usually consider constant flow-rate conditions. However, the experiments (see Bankoff & Lee 1986) are typically performed using constant pressure drop. We will discuss the differences between these two scenarios further in § 5.

The asymptotic analysis proposed above breaks down if the interfacial height h becomes too close to the upper wall. We see this when the leading-order terms in A_1 and ϵA_2 become comparable, where

$$\frac{1}{(1-h)^3} \sim \frac{\epsilon}{(1-h)^6},$$

for the constant gas volumetric flow-rate condition. Hence our theory is not applicable for the values of interfacial height such that $1-h \sim \epsilon^{1/3}$.

3. Numerical method

Before outlining the details of numerical simulation, we discuss the imposed boundary conditions on the interfacial height $h(\xi, \tau)$. Since we are not considering edge effects at the liquid inlet or liquid exit (see figure 1), we choose boundary conditions that we anticipate will be similar to what would be found in a physical experiment far away from the inlet or exit. The physical problem that includes edge effects would require a matched asymptotic expansion from the nonlinear system derived in § 2 to the transition regimes at the liquid inlet and exit. This matched asymptotic analysis will be addressed in future work. Here, we prescribe that at $\xi = 0$ (which we call the inlet), the fluid height is equal to h_-, while the height at $\xi = L$ (which we call the exit) is held fixed at h_+.

Next, we draw attention to the details of the numerical simulation and related issues. We use a finite-difference method with equally spaced grid points to solve the highly nonlinear evolution equation (2.36). The time discretization is performed by a Θ-scheme

$$\frac{h_k^{n+1} - h_k^n}{\Delta t^n} + \theta f_k^{n+1} + (1-\theta) f_k^n = 0 \qquad (k = 1, \ldots, N). \tag{3.1}$$

where $0 \leqslant \theta \leqslant 1$, n stands for the time level t^n and k corresponds to the grid point x_k and N to the total number of grid points. Here, $\theta = 0$ gives the forward Euler explicit scheme, $\theta = 1$ gives the backward Euler implicit scheme, and $\theta = 1/2$ (which we use) yields the Crank–Nicolson scheme.

Equations (3.1) form a nonlinear algebraic system of N equations, which is solved using iterative Newton–Kantorovich's method (for the description of method we refer to Diez & Kondic 2002). The idea is to linearize equations around h_k^* and obtain the system of linear equations for the correction q_k for a guess at the interfacial height h_k^*. The obtained system of linear equations leads to a five-diagonal matrix of coefficients which is solved using the biconjugate gradient method (Press *et al.* 1997). As a guess for the solution h_k^*, we use the solution at the previous time level. If the maximum value of the correction q_k is greater than the tolerance (typically, 10^{-10}), then we choose a new initial guess as $h_k^* + q_k$, $k = 1, \ldots, N$. This procedure is iteratively performed until the maximum value of the correction is less than the tolerance.

4. Admissible criteria for travelling-wave solutions

In this section, we derive *a priori* bounds for the values of $h(x, t)$ in the system without inertial effects in order to find necessary conditions under which travelling-wave solutions can be found. Note that the analysis presented here does not prove that

these solutions exists in any particular region of parameter space, but finding when the system is compatible with weak shock travelling-wave solutions helps to classify the results presented in § 5 in the context of related single-phase gravity-Marangoni flow. The rigorous existence proof is deferred to future work.

Now we briefly summarize the main conclusions of the work by Bertozzi *et al.* (1999), which analysed the model resulting from a gravity-Marangoni-driven single-phase liquid-film flow

$$h_t + (h^2 - h^3)_x = -\epsilon(h^3 h_{xxx})_x, \tag{4.1}$$

where h is the fluid thickness and ϵ is a small parameter.

The travelling-wave solutions connect an upstream height h_- to a downstream height $h_+ < h_-$, and steepen to shock wave solutions of (4.1) as $\epsilon \to 0$. If the speed s of a resulting travelling wave satisfies $\lambda(h_+) < s < \lambda(h_-)$ with $\lambda(h) = 2h - 3h^2$ then the shock is called a compressive or Lax shock. Shocks violating this condition are called undercompressive. It is found that when $h_- - h_+$ is small, the shock is compressive. As h_- increases, there are multiple travelling waves, of which two are stable and two are unstable. In this range of h_-, the stable solutions of (4.1) are found, which are composed of two waves travelling with different speeds. The slower wave corresponds to a Lax shock joining h_- to a height $h_{UC} > h_-$, where h_{UC} is independent of h_-, while the faster wave corresponds to an undercompressive shock from h_{UC} to h_+. Experimentally, the observed transition is due to a fundamental change in structure of the front, from a classical capillary shock (for negligible gravity), which is linearly unstable to perturbations, to a structure (for non-negligible gravity), that includes an 'undercompressive shock'. The undercompressive structure also manifests itself in larger bumps that continue to broaden.

4.1. *Flow driven by constant gas volumetric flow rate*

To explore conditions under which (2.36) may support travelling-wave solutions, we extend the domain to the entire plane and assume constant gas volumetric flow rate. This equation then takes the form

$$h_\tau + f_\xi + \epsilon\left[\tfrac{1}{3}Sh^3 h_{\xi\xi\xi} - \tfrac{1}{3}h^3 h_\xi \cos\beta + Re_l \bar{I}\right]_\xi = 0, \tag{4.2}$$

where

$$f(h) = \tfrac{1}{3}h^3 \sin\beta + \mu q \frac{6h^2 - 3h + 1}{(1-h)^3} + \epsilon\left[-\frac{12\mu^2 q h^3}{(1-h)^5} - \frac{\mu \sin\beta h^4(h^2+3)}{3(1-h)^3} + \frac{\mu h^2(h+3)}{(1-h)^3}\gamma\right], \tag{4.3}$$

$$\bar{I} = g(h)h_\xi, \tag{4.4}$$

with

$$g(h) = \frac{h^5(65h^2 + 665h + 112)}{140(1-h)^4}\mu q \sin\beta + \frac{3\mu^2 q^2}{35}\frac{h^5(5h^3 + 72h^2 + 392h + 245)}{(1-h)^8} + \frac{6\rho q^2}{35}\frac{h^2(27h - 10)}{(1-h)^3} + \frac{2}{15}h^6 \sin^2\beta, \tag{4.5}$$

$$\gamma = \frac{h_-^3}{3}\sin\beta + \frac{\mu q h_-^2(3 + h_-)}{(1-h_-)^3} - \frac{h^2(h+3)}{12}\sin\beta - \mu q \frac{h^3 - 3h^2 + 6h}{(1-h)^3}, \tag{4.6}$$

where γ is found from the condition that the correction to leading-order gas volumetric flow rate vanishes. Note that the capillary shock profile is a travelling-wave

solution $h(\xi - st)$ of the PDE (4.2) where s is the shock speed and satisfies the Rankine–Hugoniot condition

$$s = \frac{f(h_-) - f(h_+)}{h_- - h_+}.$$

We derive bounds on the admissible far-field states ($h_\pm$) for such a solution, if it exists. A travelling wave $h(\xi - st)$ connecting the state h_- to the state h_+ satisfies

$$-sh_\xi + f_\xi = -\alpha(h^3 h_{\xi\xi\xi})_\xi + \theta(h^3 h_\xi)_\xi - \epsilon Re_l \bar{I}_\xi, \tag{4.7}$$

where

$$\alpha = \tfrac{1}{3}\epsilon S,$$
$$\theta = \tfrac{1}{3}\epsilon \cos\beta.$$

We integrate (4.7) once to obtain

$$-sh + f = -\alpha h^3 h_{\xi\xi\xi} + \theta h^3 h_\xi - \epsilon Re_l \bar{I} + K, \tag{4.8}$$

where

$$K = -sh_+ + f(h_+).$$

To proceed, we note that any scalar conservation law of the form

$$h_t + (f(h))_x = 0 \tag{4.9}$$

can be rewritten as (see also Bertozzi *et al.* 1999)

$$\bar{G}(h)_t + F(h)_x = 0,$$

where $\bar{G}, F$ are called an entropy-entropy flux pair: $\bar{G}$ is convex and F is related to $\bar{G}$ by compatibility with the conservation law (4.9)

$$F'(h) = \bar{G}'(h) f'(h). \tag{4.10}$$

Let us apply the entropy–entropy flux pair concept to (4.2), in order to find compatibility conditions for travelling-wave solutions that connect the left-hand state h_- to the right-hand state $h_+ < h_-$. Assume that $h_+ > 0$. If we have a travelling-wave solution, $h(\xi - st)$, it must satisfy (4.7). Now we consider a function of h, $\bar{G}(h)$, that satisfies $\bar{G}''(h) > 0$ on some range of h. Multiplying (4.7) by $\bar{G}'(h)$, and integrating by parts from $-\infty$ to ∞ gives

$$-s[\bar{G}(h)] + [F] = \int \bar{G}' r(h)\,\mathrm{d}x, \tag{4.11}$$

where

$$r(h) = \epsilon\left[-\tfrac{1}{3}S\{h^3 h_{xxx}\}_x + \tfrac{1}{3}\cos\beta\{h^3 h_x\}_x - Re_l I_x\right].$$

The first term in integral (4.11)

$$\int -\tfrac{1}{3}\epsilon S\{h^3 h_{xxx}\}_x \bar{G}'\,\mathrm{d}x = \tfrac{1}{3}\epsilon S \int h^3 h_{xxx} h_x \bar{G}''\,\mathrm{d}x$$

is non-positive for $\bar{G}''(h) = h^{p-3}$ provided that p satisfies the inequality $-1/2 < p \leqslant 1$. The case $p = 1$, as in Bertozzi *et al.* (1999), gives the sharpest restriction and we obtain $\bar{G}(h) = -\ln(h)$.

The second term in integral (4.11), describing the hydrostatic pressure effects is negative for $0 < h < 1$

$$\epsilon \int \frac{\cos\beta}{3}\{h^3 h_x\}_x \bar{G}'\,\mathrm{d}x = -\epsilon\frac{\cos\beta}{3}\int \bar{G}'' h^3 h_x^2\,\mathrm{d}x. \tag{4.12}$$

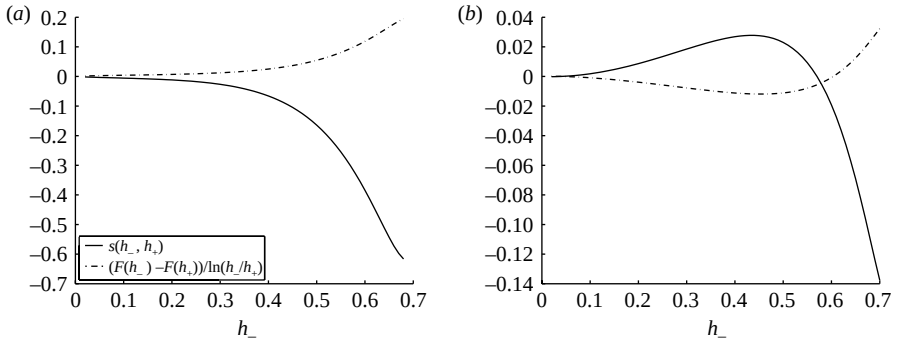

FIGURE 2. Graphs of the left- and right-hand sides of inequality (4.15) for $\epsilon = 0.01$, $\mu = 1$, $h_+ = 0.01$, $\beta = \pi/2$. (*a*) The graph ($q = -0.02$) shows that for this q, there are no admissible h_-. (*b*) The graph ($q = -0.004$) shows that for this q, the region of admissible h_- is given by $h_+ \leqslant h_- \leqslant 0.58$.

Thus, from (4.11) it follows that

$$-s[\bar{G}(h)] + [F] \leqslant 0. \tag{4.13}$$

The jump in the entropy can be written as

$$[\bar{G}] = -\ln(h_+) + \ln(h_-),$$

and the jump in the flux is

$$[F] = F(h_+) - F(h_-),$$

where (see (4.3) and (4.10))

$$F(h) = -\tfrac{1}{2}h^2 \sin\beta - 6\mu q\left[\frac{2}{3(1-h)^3} - \frac{1}{2(1-h)^2}\right] + \epsilon\left\{-6\mu C_1\left[\frac{2}{3(1-h)^3} - \frac{1}{2(1-h)^2}\right]\right\}$$
$$+ \epsilon\frac{\mu\sin\beta}{4}\left\{\frac{32}{3(1-h)^3} - \frac{32}{(1-h)^2} + \frac{23}{1-h} - 23\ln(1-h) - \frac{h(5h+28)}{2}\right\}$$
$$+ 6\epsilon\mu^2 q\left\{\frac{8}{3(1-h)^6} - \frac{14}{5(1-h)^5} - \frac{1}{(1-h)^4} + \frac{1}{3(1-h)^3} + \frac{1}{2(1-h)^2}\right\},$$

and C_1 is defined by

$$C_1 = \tfrac{1}{3}h_-^3 \sin\beta + \frac{\mu q h_-^2(3+h_-)}{(1-h_-)^3}. \tag{4.14}$$

We obtain the final inequality for the bounds for admissible capillary shocks

$$s \geqslant \frac{F(h_+) - F(h_-)}{\ln(h_-) - \ln(h_+)}. \tag{4.15}$$

Figure 2 shows the left- and right-hand sides of the inequality (4.15). For prescribed parameters of the system, and for given h_+, there are maximum and minimum values of h_- for which travelling waves may exist. If we fix ϵ, μ, β and h_+ and increase q from -0.02 (figure 2*a*) to -0.004 (figure 2*b*) then the region of admissible h_- increases from zero to the range $h_+ = 0.01 \leqslant h_- \leqslant 0.58$. The changes in the range of admissible h_- can also be caused by the variation of other parameters (e.g. μ, β), as can be seen from (4.15).

Figure 3 shows in more detail plots of the regions of admissible values of h_- for different values of q. Clearly, a decrease of q leads to the decrease of the admissible region. Therefore, our results predict that these solutions may be more easily observed

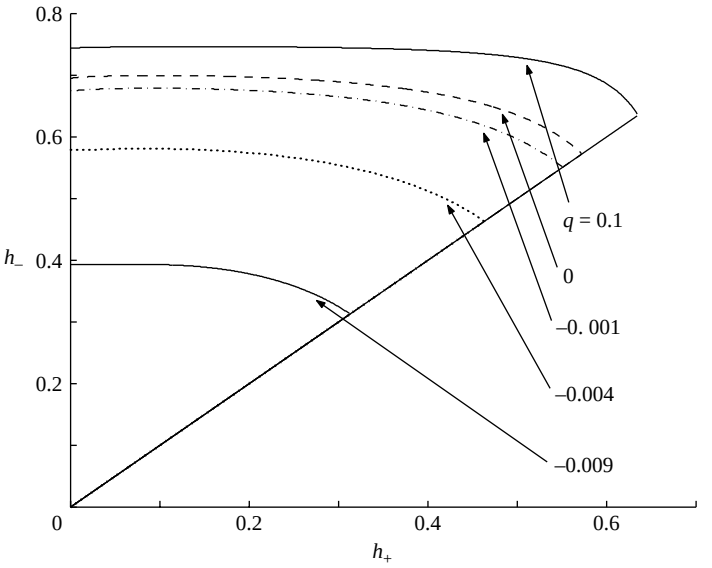

FIGURE 3. Bounds on h_+, h_- for which weak travelling-wave solutions are permissible, for constant gas volumetric flow rate $q = 0.1$, 0, -0.001, -0.004, -0.009. Weak travelling-wave solutions are not permitted outside of these ranges ($Re_l = 0$ here).

in the system characterized by a smaller absolute value of q, for $q < 0$. In addition, for $q > 0$ (corresponding to cocurrent downstream flow) we observe that the region of admissible travelling-wave solutions is even larger.

4.2. *Flow driven by constant pressure drop*

Next, we consider the flow driven by constant pressure drop. Here, instead of (4.2), we obtain the following equation

$$h_\tau + A_1(h, \Delta P)h_\xi + \epsilon[SC(h)h_{\xi\xi\xi} + A_2(h, \Delta P) + Re_l I(h, \Delta P) + P(h)h_\xi]_\xi = 0, \quad (4.16)$$

where

$$A_1(h, \Delta P) = h^2 \sin\beta - \frac{h(h+1)\Delta P}{2(1-h)^4 \int_0^1 \mathrm{d}\xi/(1-h)^3}, \quad (4.17)$$

$$C(h) = \tfrac{1}{3}h^3, \quad P(h) = -\tfrac{1}{3}h^3 \cos\beta,$$

$$A_2(h, \Delta P) = -\frac{\mu h^3 \Delta P}{4(1-h)^4 \int_0^1 \mathrm{d}\xi/(1-h)^3} - \frac{\mu h^4}{4(1-h)} \sin\beta$$

$$+ \frac{\mu h^2(h+3)}{(1-h)^3} \left[\gamma - \frac{h^2(h+3)}{12} \sin\beta - \frac{h\Delta P}{4(1-h)^2 \int_0^L \mathrm{d}\xi/(1-h)^3} \right],$$

$$I(h, p_{0\xi}) = I_l + I_g,$$

with

$$I_l = \frac{h^4(7h+25)}{240} p_{0\xi\tau} + \frac{h^5 h_\xi}{15} \left\{ 2h \sin^2\beta + \frac{56+49h-41h^2}{56(1-h)^4 \displaystyle\int_0^L \mathrm{d}\xi/(1-h)^3} \Delta P \sin\beta \right.$$
$$\left. - \frac{(10h^2+7h+77)}{224(1-h)^7} \left[\frac{\Delta P}{\displaystyle\int_0^L \mathrm{d}\xi/(1-h)^3} \right]^2 \right\}, \quad (4.18)$$

$$I_g = \frac{h^2(27h-10)}{840(1-h)^3} \frac{h_\xi \rho}{\mu^2} \left[\frac{\Delta P}{\displaystyle\int_0^L \mathrm{d}\xi/(1-h)^3} \right]^2, \quad (4.19)$$

where

$$\gamma = -\frac{\Delta P}{\displaystyle\int_0^L \mathrm{d}\xi/(1-h)^3} \int_0^\xi \frac{h(h+1)h_{\hat\xi}}{2(1-h)^4} \,\mathrm{d}\hat\xi. \quad (4.20)$$

The integral term depends on the unknown interfacial height h. Therefore, we cannot perform an analysis similar to the case of constant gas volumetric flow rate. Instead, we resort to numerical simulations.

5. Numerical simulation

In this section we first consider the interfacial dynamics of the flow driven by a constant gas volumetric flow rate, and then analyse the influence of the inertia on the solution profile. Finally, we discuss the interfacial dynamics in the flow driven by a constant pressure drop. We note that for all of the presented results, the interfacial slopes $h_\xi = O(1)$; therefore, the lubrication approximation remains valid for all the results shown.

5.1. *Constant gas volumetric flow rate without inertial effects*

The numerical simulations are performed in a fixed (laboratory) frame. All cases use $Re_l = 0$, $q = -0.004$, $h_+ = 0.1$, $\rho = \mu = 1$, $S = 3$, $\beta = \pi/2$; the same qualitative dynamics emerge for all h_+ that are in the admissible (q-dependent) range presented in figure 3. The length of the domain is typically fixed to the value of 60, although some cases require the extended domain of length 200. For better visual presentation, we typically show in the figures the $[0:50]$ part of the domain. In each case, we consider a range of left-hand states h_- for which the dynamics of the governing PDE, (4.2), has a certain characteristic behaviour. These cases are analogous to those investigated by Bertozzi *et al.* (1999) for a model describing the interfacial dynamics of a single fluid phase driven by a thermal gradient with counteracting gravitational force. We note that the values h_1, h_2 and h_{UC} discussed below all depend upon the particular choice of system parameters and the right-hand state h_+.

Case 1: $h_+ < h_- < h_1$: *unique weak Lax shock*

Given h_+, there is a value h_1 such that for all $h_+ < h_- < h_1$, the solution of the PDE, (4.2), evolves to a unique capillary shock profile connecting the states h_- and

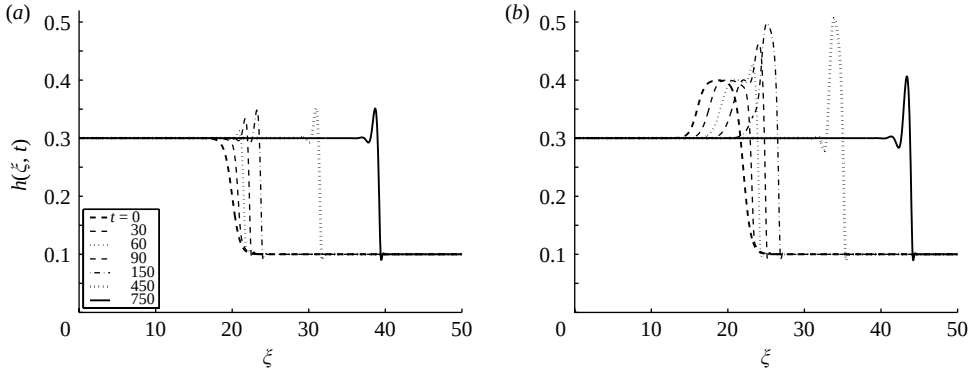

FIGURE 4. (Case 1) Interfacial profile with unique Lax shock for $q = -0.004$, $\epsilon = 0.01$, $\beta = \pi/2$, $\rho = \mu = 1$, $S = 3$, $h_- = 0.3$, $h_+ = 0.1$. Solution at later times ($t > 150$) settles down to the steady Lax shock. Here we use (a) the initial condition (5.1), and (b) the initial condition (5.2).

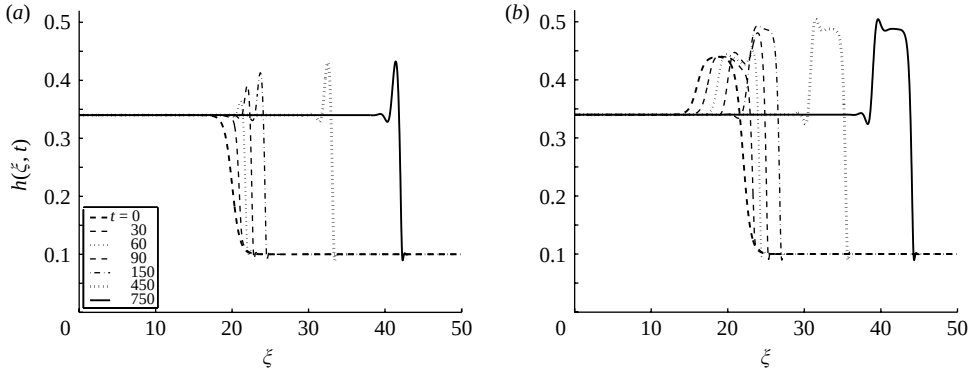

FIGURE 5. (Case 2) (a) Interfacial profiles resulting in steady Lax shock for $h_- = 0.34$ and other parameters as in figure 4 using the initial condition (5.1). (b) Double shock wave profile at different times for the same parameters as in (a) using the initial condition (5.2). Note that this double shock structure is no longer steady since the capillary ridge broadens in width.

h_+. To check this claim, we consider two initial profiles

$$h_0(\xi) = [\tanh(-\xi + 20) + 1]\frac{h_- - h_+}{2} + h_+, \tag{5.1}$$

and

$$h_0(\xi) = \begin{cases} \frac{1}{2}(h_+ - h_-)\tanh(\xi - 16) + \frac{1}{2}(h_+ + h_-) & \text{if} \quad \xi < 19, \\ -\frac{1}{2}(h_+ - h_-)\tanh(\xi - 22) + \frac{1}{2}(h_+ + h_-) & \text{if} \quad \xi > 19, \end{cases} \tag{5.2}$$

connecting the states h_- and h_+. Figure 4 shows that the solutions settle down to the unique steady travelling-wave solution, independent of the initial condition. We note that figure 4(b) still shows the transient part of the evolution; for long times, the height of the Lax shock in figure 4(b) is the same as shown in figure 4(a).

Case 2: $h_1 < h_- < h_2$: *multiple Lax shocks*

For h_- in the range $h_1 < h_- < h_2$, there are multiple weak shock profiles connecting the same two left-hand (h_-) and right-hand (h_+) states. Figure 5 shows several solutions connecting h_+ and $h_- = 0.34$. Depending on whether the initial conditions

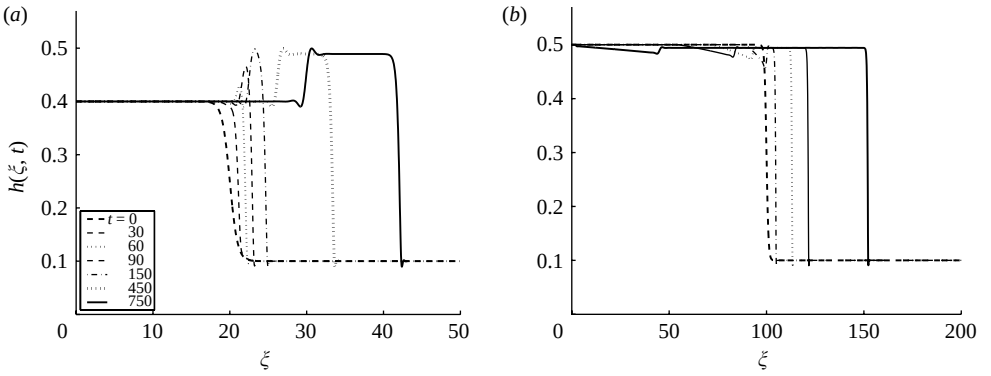

FIGURE 6. (*a*) (Case 3) Undercompressive double shock structure dynamics for $h_- = 0.4$ and other parameters as in figure 4, with the initial condition (5.1) (identical result is obtained if (5.2) is used). (*b*) (Case 4) Interfacial profile for $h_- = 0.5$ and other parameters as in figure 4 (note longer times and larger domain).

(5.1) or (5.2) are used, we obtain either the single Lax shock or double shock structure, evolving into the undercompressive shock (leading shock) and Lax shock (trailing shock). The trailing shock moves with a slower speed than the leading shock. Owing to the difference in speeds of propagation, the capillary ridge broadens.

Case 3: $h_2 < h_- < h_{UC}$: *undercompressive double shock structure*

For h_- in this range, there are no single Lax shock profiles joining h_- and h_+. All initial conditions converge to a solution with the same double shock structure. Figure 6(*a*) illustrates this behaviour for $h_- = 0.4$. The solution at the later time is characterized by the presence of two shocks. The leading shock is the undercompressive shock while the trailing shock is a classical Lax shock. We note that these are not steady travelling-wave solutions, since the width of the capillary ridge grows in time. This double shock wave structure persists for $h_- < h_{UC}$.

Case 4: $h_- > h_{UC}$: *rarefaction-undercompressive shock*

For $h_- > h_{UC}$, we obtain a two-wave structure in which the slower wave is a rarefaction wave solution. Note that these simulations are performed in larger domain in order to analyse the dynamics for longer times. Here, we use $h_- = 0.5$ and the initial condition

$$h_0(\xi) = [\tanh(-\xi + 170) + 1]\frac{h_- - h_+}{2} + h_+,$$

(we shift the initial condition (5.1) so as to be able to follow the dynamics for longer times). Figure 6(*b*) shows a combination of a rarefaction wave and an undercompressive shock. Since the undercompressive shock moves with a speed $s(h_{UC}, h_+)$, which is greater than the speed $f'(h_{UC})$ of the right-hand side (leading edge) of the rarefaction wave, the undercompressive shock separates from the rarefaction wave to produce a separated rarefaction shock profile.

Figure 7 shows the dependence of the liquid flow rate (Q_l) on h_- as gas volumetric flow rates are varied. For negative, but small q (e.g. $q = -0.0001$), Q_l is positive for all values of h_-, and this regime is countercurrent. For sufficiently large absolute values of negative q (e.g. $q = -0.01$), Q_l is negative for all values of h_-, and the flow regime is cocurrent, but in the direction opposite to gravity. However, for the intermediate values of q, Q_l can be either positive or negative. The exact value of

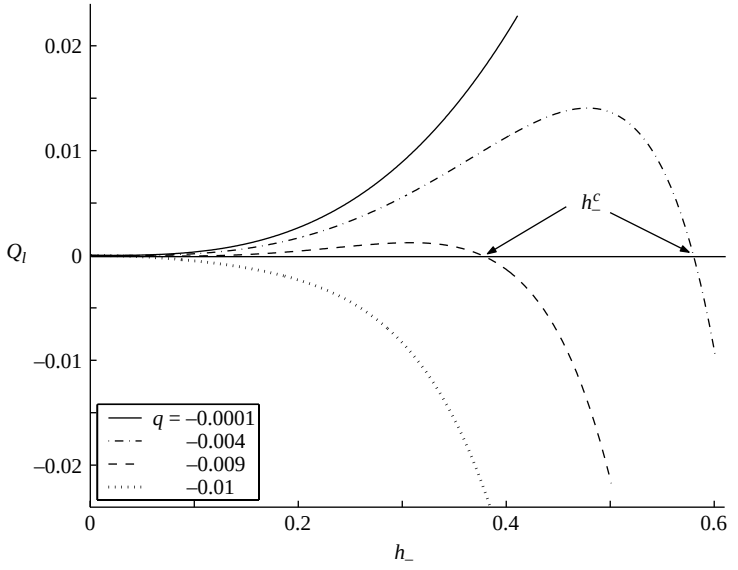

FIGURE 7. The dependence of the liquid flow rate, Q_l on h_- for fixed gas volumetric flow rate. Note the change from countercurrent flow for $q = -0.0001$ to cocurrent upstream flow for $q = -0.01$.

$h_- = h^c_-$ where Q_l changes sign depends on q, but it is typically close to the boundary of the admissible region, as can be seen by comparison with figure 3. Note that this particular regime (where Q_l changes sign) can be characterized by the presence of an inflection point in this liquid volumetric flow-rate curve. We note that in Tilley *et al.* (1994), a laminar flooding criterion was proposed for spatially periodic solutions that correspond to the values of h near this inflection point. Thus, we find consistency of our results with the laminar flooding criterion of Tilley *et al.* (1994*b*). Our numerical results imply that the existence of an inflection point is also the requirement for the formation of a double shock structure. We expect that the liquid flow reversal, and related formation of double shock structures, are related to the onset of flooding (Dukler & Smith 1979).

Figure 8 summarizes all our numerical simulations presented so far. In this figure, for particular values of $q = -0.004$, $S = 3$, $\epsilon = 0.01$, $\mu = \rho = 1$, $\beta = \pi/2$, we plot the regions where the four cases considered above appear. Note that numerically found values of h_1, h_2 and h_{UC} for case $h_+ = 0.1$ are different from the corresponding values of h_1, h_2 and h_{UC} for $h_+ = 0.2$ and $h_+ = 0.3$. We observe that an increase of h_+ leads to a decrease of the size of regions where we obtain unique Lax shock, multiple Lax shocks, double shock structure, or a combination of rarefaction wave and undercompressive shock.

5.2. *Constant gas volumetric flow rate including inertial effects*

We now consider the role of the inertia of the denser layer on the interfacial dynamics. Figure 9 shows the profiles in the countercurrent flows with and without inertial effects. In this case of countercurrent flow, the presence of fluid inertia influences neither the interfacial profiles, nor the speed of propagation. Similar results were found in other countercurrent-flow cases. In the case of cocurrent downstream flow, however, we observe that inertia does influence the transient behaviour of the interfacial profile. Still, the final state is insensitive to the presence of inertia. Figure 10 shows the

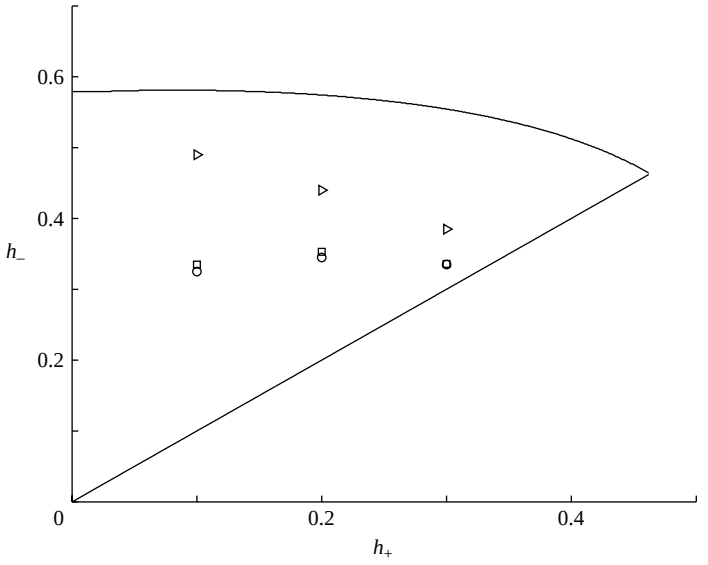

FIGURE 8. Regions for admissible travelling shock solutions for $q = -0.004$ and other parameters as in figure 4. ○, h_1; □, h_2; ▷, combination of rarefaction and undercompressive waves. The solid line is copied from figure 3.

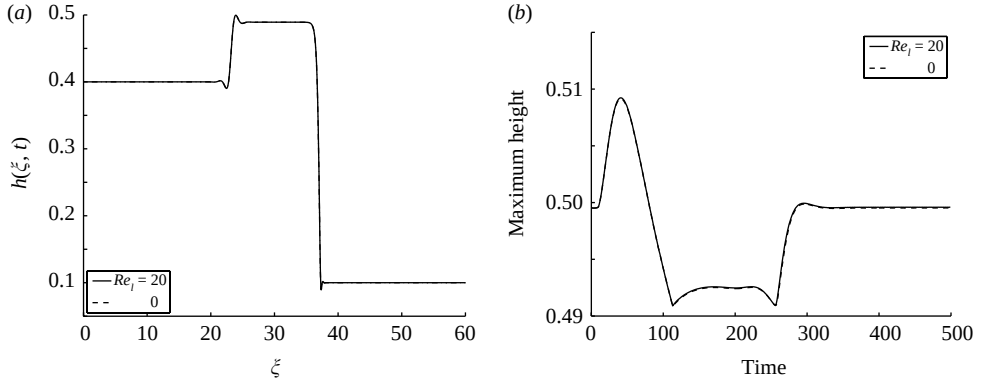

FIGURE 9. (*a*) Interfacial profiles for constant gas volumetric flow rate case without inertia ($Re_l = 0$) and with inertia ($Re_l = 20$) at time $t = 750$ for $q = -0.004$, $h_- = 0.4$ and other parameters as in figure 4. (*b*) Change of interfacial height in time without and with inertia. The overlap of the lines in both figures shows that the influence of inertia is negligible.

interfacial proiles for this case, with positive gas volumetric flow rate ($q = 0.0001$) when inertial effects are included ($Re_l = 20$, solid line), or not ($Re_l = 0$, dashed line). We see that the position of the classical Lax shock at the time $t = 500$ is the same in these two cases, although the height of the transient profile changes more slowly in the presence of liquid inertia. We have also verified numerically that the fluid inertia does not change the boundaries of the shock travelling-wave regions, shown in figure 8.

5.3. *Flow driven by constant pressure drop*

Next, we consider the case of constant pressure drop and allow the gas volumetric flow rate to vary in time. (Note that incompressibility of both fluids requires that the

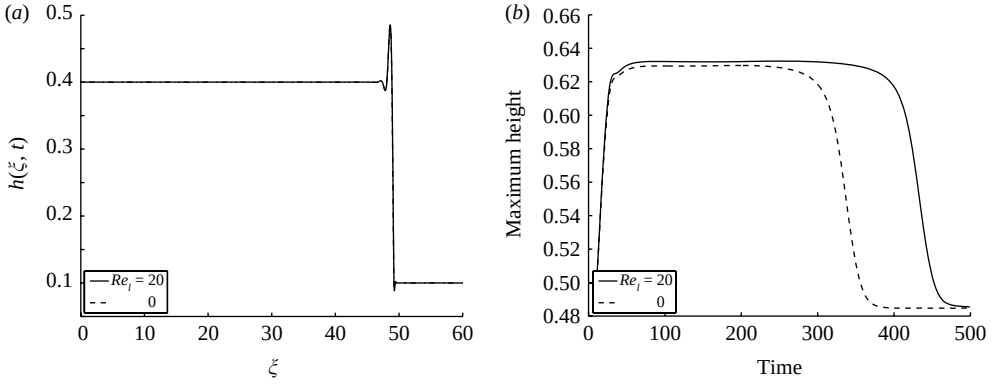

FIGURE 10. (*a*) Interfacial profiles for constant gas volumetric flow rate case without inertia ($Re_l = 0$, dashed line) and with inertia ($Re_l = 20$, solid line) at time $t = 500$ using $q = 0.0001$ (cocurrent flow), $h_- = 0.4$ and other parameters as in figure 4. (*b*) Change of the maximum of interfacial height in time. At time $t = 500$, the profiles in both cases (without and with inertia) coincide.

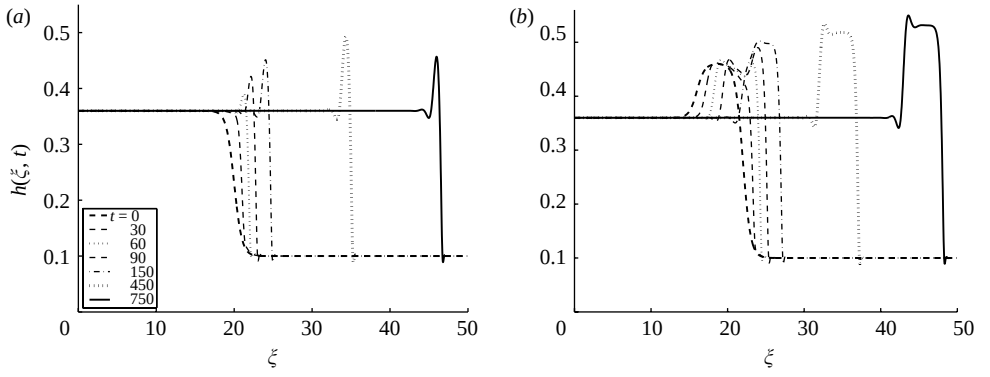

FIGURE 11. (Case 2) Profiles of travelling double-shock wave solution for constant pressure drop case (ΔP is chosen so it corresponds to $q = -0.004$ at time $t = 0$) without inertia using system parameters as in figure 4 and $h_- = 0.36$.

total flow rate remains constant.) We describe the dynamics in the context of the fixed gas volumetric flow rate from § 5.1. Since some of the results are very similar to those from § 5.1, we present in this section only the figures which illustrate the differences between these two cases.

Case 1. Interfacial profiles in this regime appear to be identical to the fixed gas volumetric flow rate.

Case 2. The shape of the interfacial patterns (figure 11) resembles the qualitative features of those found in the fixed gas volumetric flow rate. For initial conditions given in (5.1), the transients eventually evolve to the steady travelling Lax shock solution. For initial condition given in (5.2), the double-shock structure results. However, the maximum value increases as the structure evolves, in contrast to the constant gas volumetric flow rate case shown in figure 5(*b*). This growth of the maximum value is shown in figure 12, which compares the maximum height of the interface for the constant pressure drop case (solid line) and for the constant gas volumetric flow rate (dashed line).

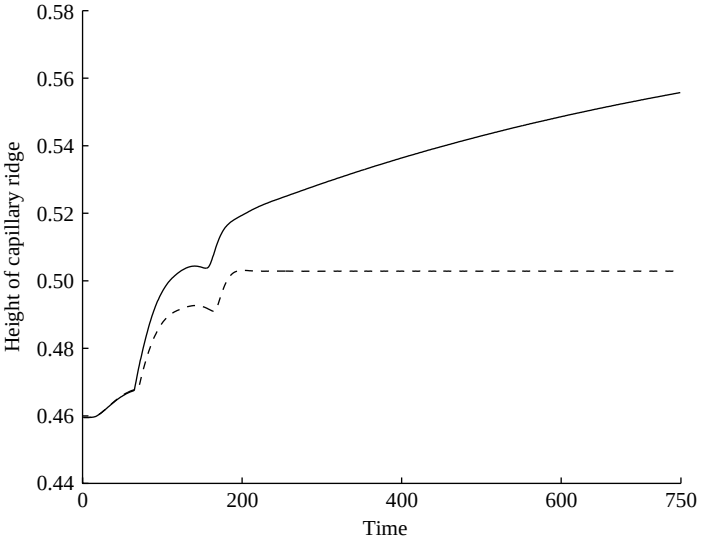

FIGURE 12. Height of the undercompressive shock versus time for constant pressure drop (solid) and constant gas volumetric flow rate (dashed) using $h_- = 0.36$, the initial condition (5.2) and other parameters as in figure 4. The corresponding interfacial profile for the constant pressure drop case is shown in figure 14 and for the constant gas volumetric flow rate in figure 9. After initial transients, we see steady increase of the height of the shock in the case of the flow driven by constant pressure drop.

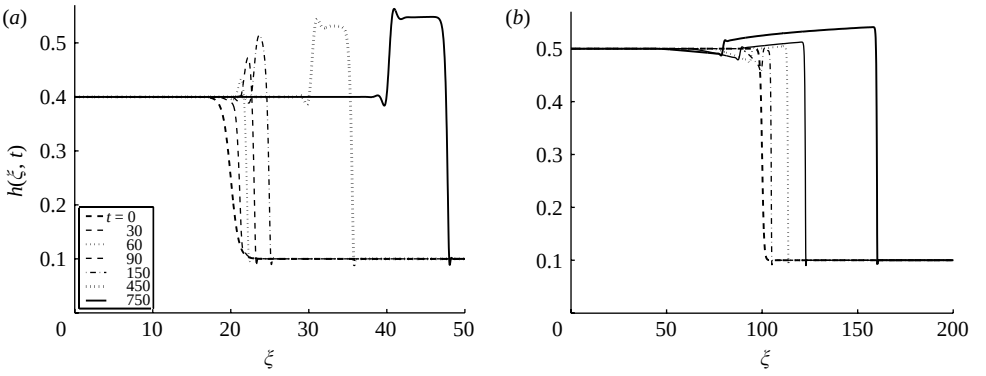

FIGURE 13. (*a*) (Case 3) Undercompressive double-shock structure dynamics for constant pressure drop case (ΔP is chosen so it corresponds to $q = -0.004$ at time $t = 0$) using $h_- = 0.4$ and other parameters as in figure 4 (compare figure 6*a*). (*b*) (Case 4) Interfacial profiles for $h_- = 0.5$ and other parameters as in figure 4. (compare figure 6*b*; note longer times and larger domain).

Case 3. Figure 13(*a*) shows the double-shock structure which is similar to that found in the fixed gas volumetric flow rate. Similarly to Case 2, we find that the maximum height increases, in contrast to the constant gas flow-rate case (see figure 6*a*).

Case 4. Figure 13(*b*) depicts the interfacial profiles evolving into the combination of rarefaction and undercompressive waves ($h_- = 0.5$). Again, the transient behaviour differs from the fixed gas volumetric flow-rate case. The rarefaction wave appears to evolve as earlier (see figure 6*b*). However, the double shock evolves with the forward peak growing in time while the maximum located near the Lax shock remains close to $h = 0.5$.

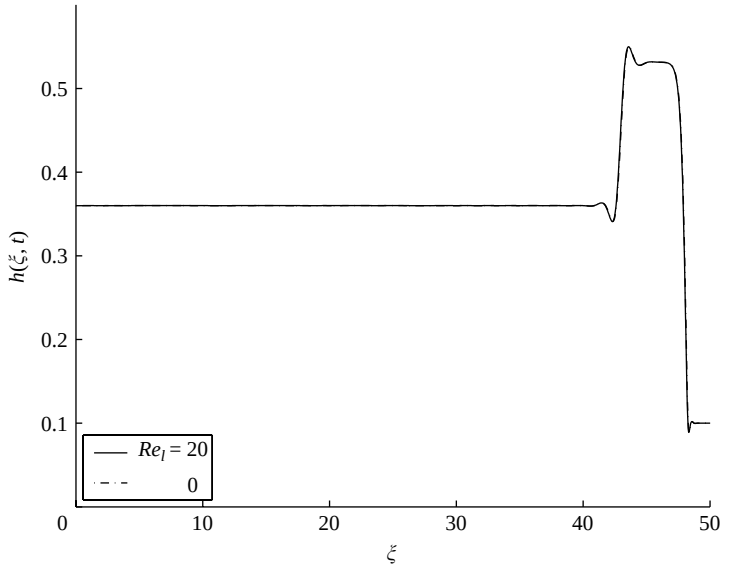

FIGURE 14. Interfacial dynamics of travelling shock-wave solution for constant pressure drop case (initially corresponding to $q = -0.004$) without inertia ($Re_l = 0$) and with inertia ($Re_l = 20$), $h_- = 0.36$, $t = 750$ and other parameters as in figure 4. Clearly, the influence of inertia is negligible.

5.4. *Constant pressure drop with inertia*

In all of the cases we have investigated, no quantitative changes were found as a result of inertial effects. An example of this is shown in figure 14, where interfacial profiles for countercurrent constant pressure flow with and without inertia are compared. Notice that the profiles appear to be unchanged, up to the resolution of the plot.

6. Conclusions

In this work, we have investigated the nonlinear evolution of the interface between two incompressible immiscible fluids in an inclined channel. Our study is motivated by air–water systems, and therefore we consider the fluids which have disparate dynamic viscosities and densities. Through a lubrication approximation, we derive a system of nonlinear evolution equations that govern the interfacial motion between the two fluids and the leading-order pressure contribution. The lubrication approach includes the inertial effects of both the liquid and gas layers.

We consider two different forcing scenarios. The first, where the gas volumetric flow rate is fixed, results in a standard lubrication approximation, and the interfacial dynamics depends only on local variations of the interfacial shape. We find that the undercompressive shock paradigm found in Marangoni-driven fluid layers is qualitatively applicable in the countercurrent flow regime in our case. Small differences in the upstream and downstream interfacial height result in the formation of Lax shocks. Larger differences result in bistability among Lax shocks and unsteady double-shock structures. This bistability is lost when this differential is increased (double-shock structures are stable and Lax shocks are unstable). Finally, a solution forms which combines the double shock and a rarefaction wave.

The second scenario, where the pressure difference over the channel length is fixed, results in a non-local dependence of the interfacial dynamics on the interfacial shape.

Although the regimes outlined above persist in the flow driven by constant pressure drop, the interfacial heights change in time as the shocks propagate downstream, and, in particular, we observe the growth of the undercompressive shock height. Therefore, the travelling-wave solutions found in the constant gas volumetric flow rate case do not exist for the flow driven by constant pressure drop. This is the main difference between these two scenarios.

Although our theory and numerical simulation cannot quantify the dynamics completely in the case of constant pressure drop, a theory that allows for inertial effects that are comparable to surface-tension effects may be able to capture the final state of this transient behaviour. This transient may be related to a flooding scenario, since the liquid and gas volumetric flow rates in this case are the same as the dynamic flooding criterion found in Tilley *et al.* (1994*b*) for the spatially periodic system.

Finally, we reiterate that we have only considered one particular set of fluids and a simple geometry (vertical channel) in some detail, in order to focus on how the flow constraints (either local or non-local) can affect the dynamics of the flow. The applied constraints and boundary conditions on the interfacial height that we have used in this study are approximations of what we anticipate to be true in experiment. One clear outcome of this study is that a proper mathematical description of the correct experimental conditions is vital in order to understand the physical mechanisms for onset of flooding.

B. S. T. & T. M. S. are supported by NSF under grant number DMS-9971383. Partial support by grant number NSF INT-0122911 is also acknowledged. T. M. S. thanks Olin College for their support.

Appendix A. Derivation of the evolution equation

At $O(\epsilon)$, the x-momentum and continuity equations (2.6)–(2.7) yield

$$Re_l\left(u_{0\tau}^{(1)} + u_0^{(1)}u_{0\xi}^{(1)} + u_{0\zeta}^{(1)}w_0^{(1)}\right) = -p_{1\xi}^{(1)} + u_{1\zeta\zeta}^{(1)}, \tag{A 1}$$

$$Re_l\rho\left(u_0^{(2)}u_{0\xi}^{(2)} + u_{0\zeta}^{(2)}w_0^{(2)}\right) = -p_{1\xi}^{(2)} + \mu u_{1\zeta\zeta}^{(2)}, \tag{A 2}$$

$$u_{1\xi}^{(1)} + w_{1\zeta}^{(1)} = 0, \tag{A 3}$$

$$u_{1\xi}^{(2)} + w_{1\zeta}^{(2)} = 0, \tag{A 4}$$

$$u_1^{(1)} = 0 \qquad (\zeta = 0), \tag{A 5}$$

$$u_1^{(2)} = 0 \qquad (\zeta = 1), \tag{A 6}$$

$$w_1^{(1)} = 0 \qquad (\zeta = 0), \tag{A 7}$$

$$w_1^{(2)} = 0 \qquad (\zeta = 1), \tag{A 8}$$

$$\mu u_{1\zeta}^{(2)} - u_{1\zeta}^{(1)} = 0 \qquad (\zeta = h(\xi, \tau)), \tag{A 9}$$

$$w_1^{(2)} - h_\xi u_1^{(2)} - w_0^{(1)} + h_\xi u_0^{(1)} = 0 \qquad (\zeta = h(\xi, \tau)). \tag{A 10}$$

Using equations (A 1)–(A 4) and the boundary and interfacial conditions (A 5)–(A 9), similar to the analysis at the previous order, we arrive at the solution for $u_1^{(i)}$

$$u_1^{(1)} = P_{1\xi}\frac{\zeta^2}{2} + \phi\zeta + F^{(1)}(\xi, \zeta, \tau), \tag{A 11}$$

$$u_1^{(2)} = \frac{P_{1\xi} + \alpha}{2\mu}(\zeta - 1)^2 + \psi(\zeta - 1) + F^{(2)}(\xi, \zeta, \tau), \tag{A 12}$$

where

$$\phi = \mu F_{\zeta}^{(2)}(\xi, h, \tau) - F_{\zeta}^{(1)}(\xi, h, \tau) - \frac{\mu}{h-1} F^{(2)}(\xi, h, \tau) + \frac{\mu h}{2(h-1)} \{h \sin\beta - p_{0\xi}\} + \alpha \frac{h-1}{2} - P_{1\xi} \frac{h+1}{2}, \quad \text{(A 13)}$$

$$\psi = \frac{F^{(2)}(\xi, h, \tau)}{1-h} + \frac{(P_{1\xi} + \alpha)(1-h)}{2\mu} + \frac{h(h \sin\beta - p_{0\xi})}{2(h-1)}, \quad \text{(A 14)}$$

$$\alpha = Sh_{\xi\xi\xi} - h_{\xi} \cos\beta. \quad \text{(A 15)}$$

We refer to Appendix B for the definition of the inertial terms $F^{(i)}$. The continuity of normal velocity (2.10) then gives the equation for the pressure gradient

$$[p_{0\xi}(h-1)^3 + \epsilon\{(h-1)^3(P_{1\xi} + \alpha) + 12\mu\theta\}]_{\xi} = \epsilon \frac{6\mu h(h+1)}{(1-h)} h_{\xi} p_{0\xi}$$

where

$$\theta = \frac{h^2(h+3)}{12} \sin\beta + \frac{h(h-1)}{4} p_{0\xi} - \frac{17}{3360} Re_l \frac{\rho}{\mu^3} h_{\xi} p_{0\xi}^2.$$

Appendix B. Derivation of the inertial terms $F^{(i)}(\xi, \zeta, \tau)$

To find the inertial term $F^{(2)}(\xi, \zeta, \tau)$ in (A 11) and (A 12) we must solve the problem:

$$F_{\zeta\zeta}^{(2)}(\xi, \zeta, \tau) = Re_l \frac{\rho}{\mu} \left(u_0^{(2)} u_{0\xi}^{(2)} + u_{0\zeta}^{(2)} w_0^{(2)}\right), \quad \text{(B 1)}$$

$$F^{(2)}(\xi, 1, \tau) = 0, \quad \text{(B 2)}$$

$$F_{\zeta}^{(2)}(\xi, 1, \tau) = 0. \quad \text{(B 3)}$$

After integrating (B 1) and, using the boundary conditions (B 2) and (B 3), we obtain:

$$F^{(2)}(\xi, \zeta, \tau) = a_1^{(2)}(\zeta - 1)^6 + a_2^{(2)}(\zeta - 1)^5 + a_3^{(2)}(\zeta - 1)^4, \quad \text{(B 4)}$$

$$a_1^{(2)} = Re_l \frac{\rho h_{\xi} p_{0\xi}^2}{120\mu^3(1-h)}, \quad \text{(B 5)}$$

$$a_2^{(2)} = Re_l \frac{\rho h_{\xi} p_{0\xi}^2}{80\mu^3}, \quad \text{(B 6)}$$

$$a_3^{(2)} = \frac{\rho h_{\xi} p_{0\xi}^2}{48\mu^3}(1-h). \quad \text{(B 7)}$$

Similarly for $F^{(1)}(\xi, \zeta, \tau)$ we have:

$$F_{\zeta\zeta}^{(1)}(\xi, \zeta, \tau) = Re_l \left[u_{0\tau}^{(1)} + u_0^{(1)} u_{0\xi}^{(1)} + u_{0\zeta}^{(1)} w_0^{(1)}\right], \quad \text{(B 8)}$$

with the following boundary conditions:

$$F^{(1)}(\xi, 0, \tau) = 0, \quad \text{(B 9)}$$

$$F_{\zeta}^{(1)}(\xi, 0, \tau) = 0. \quad \text{(B 10)}$$

After integrating (B 8) and applying the boundary conditions (B 9) and (B 10), we obtain:

$$F^{(1)}(\xi, \zeta, \tau) = a_1^{(1)}\zeta^6 + a_2^{(1)}\zeta^5 + a_3^{(1)}\zeta^4 + a_4^{(1)}\zeta^3, \quad \text{(B 11)}$$

where

$$a_1^{(1)} = Re_l \frac{p_{0\xi\xi}}{360}(p_{0\xi} - \sin\beta),$$

$$a_2^{(1)} = Re_l \frac{p_{0\xi\xi}}{60}\left\{h\sin\beta - \frac{p_{0\xi}}{2}(h+1)\right\},$$

$$a_3^{(1)} = Re_l \frac{1}{24}\left\{p_{0\xi\tau} + \left[h\sin\beta - \frac{p_{0\xi}}{2}(h+1)\right]\left[h_\xi \sin\beta - \frac{p_{0\xi\xi}}{2}(h+1) - \frac{p_{0\xi}h_\xi}{2}\right]\right\},$$

$$a_4^{(1)} = Re_l \frac{2h_\tau \sin\beta - p_{0\xi\tau}(h+1) - h_\tau p_{0\xi}}{12}. \qquad \text{(B 12)}$$

REFERENCES

Bankoff, S. G. & Lee, S. C. 1986 Multiphase science and technology. A critical review of the flooding literature (ed. G. F. Hewitt, J. M. Delhaye & N. Zuber). Hemisphere.

Benjamin, T. B. 1957 Wave formation in laminar flow down an inclined plane. *J. Fluid Mech.* **2**, 554–574.

Bertozzi, A. L., Münch, A., Fanton, X. & Cazabat, A. M. 1998 Contact line stability and 'undercompressive shocks' in driven thin film flow. *Phys. Rev. Lett.* **81**, 5169–5172.

Bertozzi, A. L., Münch, A. & Shearer, M. 1999 Undercompressive shocks in thin film flows. *Physica* D **134**, 431–464.

Boomkamp, P. A. M. & Miesen, R. H. M. 1996 Classification of instabilities in parallel two-phase flow. *Intl J. Multiphase Flow* **22**, 67–88.

Bousman, W. S., McQuillen, J. B. & Witte, L. C. 1996 Gas–liquid flow patterns in microgravity: effects of tube diameter, liquid viscosity and surface tension. *Intl J. Multiphase Flow* **22**, 1035–1053.

Carles, P. & Cazabat, A. M. 1993 The thickness of surface-tension-gradient-driven spreading films. *J. Colloid Interface Sci.* **157**, 196–201.

Chang, H.-C. 1986 Nonlinear waves on liquid film surfaces. Part I: Flooding in a vertical tube. *Chem. Engng Sci.* **41**, 2463–2476.

Diez, J. A. & Kondic, L. 2002 Computing three dimensional thin film flows including contact lines. *J. Comput. Phys.* **183**, 274–306.

Duenckel, R. 2002 Improved fracture conductivity brings value to hydraulic fracturing. *Am. Oil Gas Rep.*

Dukler, A. E., Fabre, J. A., McQuillen, J. B. & Vernon, R. 1988 Gas liquid flow at microgravity conditions: flow patterns and their transitions. *Intl J. Multiphase Flow* **14**, 389–400.

Dukler, A. E. & Smith, L. 1979 Two-phase interactions in countercurrent flow: studies of the flooding mechanism. *NUREG/CR-0617* Nuclear Regulatory Commission, Washington, DC.

Floryan, J. M., Davis, S. H. & Kelly, R. E. 1987 Instabilities of a liquid film flowing down a lightly inclined channel. *Phys. Fluids* **30**, 983–989.

Fowler, A. C. & Lisseter, P. E. 1992 Flooding and flow reversal in annular two-phase flows. *SIAM J. Appl. Maths* **52**, 15–33.

Joo, S. W., Davis, S. H. & Bankoff, S. G 1991 Long-wave instabilities of heated falling films. *J. Fluid Mech.* **230**, 117–146.

Joseph, D. D. & Renardy, Y. Y. 1992 Fundamentals in two-fluid dynamics, Part I: Mathematical Theory and Applications. Springer.

Kataoka, D. E. & Troian, S. M. 1999 Patterning liquid flow on the microscopic scale. *Nature* **402**, 794–797.

Kluwick, A., Cox, E. A. & Scheichl, S. 2000 Non-classical kinematic shocks in suspensions of particles in fluids. *Acta Mech.* **144**, 197–210.

Kouris, C. & Tsamopoulos, J. 2002 Dynamics of the axisymmetric core–annular flow. II. The less viscous fluid in the core, saw tooth waves. *Phys. Fluids* **13**, 1011–1029.

Ludviksson, V. & Lightfoot, E. N. 1971 The dynamics of thin liquid films in the presence of surface-tension gradients. *AIChE J.* **17**, 1166–1173.

Moritis, G. 2001 Flow assurance challenges production from deeper water. *Oil Gas J.* **99**, 66–69.

Münch, A. 2003 The pinch-off transition in Marangoni driven thin films. *Phys. Rev. Lett.* **91**, 016105-1–4.

Pettigrew, K., Kirshberg, J., Yerkes, K., Trebotich, D. & Liepmann, D. 2001 Performance of a MEMS based micro capillary pumped loop for chip-level temperature control. *IEEE* 427–430.

Press, W. H., Teukolsky, S. A., Vetterling, W. T. & Flannery, B. P. 1997 *Numerical Recipes in Fortran 77. The Art of Scientific Computing* (vol. 1 of Fortran Numerical Recipes), Cambridge University Press.

Schneemilch, M. & Cazabat, A. M. 2000*a* Wetting films in thermal gradients. *Langmuir* **16**, 8796–8801.

Schneemilch, M. & Cazabat, A. M. 2000*b* Shock separation in wetting films driven by thermal gradients. *Langmuir* **16**, 9850–9856.

Smith, M. K. 1990 The mechanism for the long-wave instability in thin liquid films. *J. Fluid Mech.* **217**, 469–486.

Stone, H. A., Stroock, A. D. & Ajdari, A. 2004 Engineering flows in small devices: microfluidics toward a lab-on-a-chip. *Annu. Rev. Fluid Mech.* **36**, 381–411.

Sur, J., Bertozzi, A. L. & Behringer, R. P. 2003 Reverse undercompressive shock structures in driven thin film flow. *Phys. Rev. Lett.* **90**, 126105-1–4.

Tilley, B. S., Davis, S. H. & Bankoff, S. G. 1994*a* Linear stability theory of two-layer fluid flow in an inclined channel. *Phys. Fluids* A **6**, 3906–3922.

Tilley, B. S., Davis, S. H. & Bankoff, S. G. 1994*b* Nonlinear long-wave stability of superposed fluids in an inclined channel. *J. Fluid Mech.* **277**, 55–83.

Yih, C.-S. 1967 Instability due to viscosity stratification. *J. Fluid Mech.* **27**, 337–352.

Zhang, J., Miksis, M. J., Bankoff S. G. & Tryggvason, G. 2002 Nonlinear dynamics of an interface in an inclined channel. *Phys. Fluids* **14**, 1877–1885.